

Fewest-Switches Surface Hopping with Combined Deep Learning Potential and Long Short-Term Memory Network Propagator for Simulating Realistic Photochemical Processes

Zhenxing Zhu,[†] Diandong Tang,^{*,†} Lin Shen,^{*,†} and Wei-Hai Fang[†]

[†]*Key Laboratory of Theoretical and Computational Photochemistry of Ministry of Education, College of Chemistry, Beijing Normal University, Beijing 100875, China;*

[‡]*Department of Chemistry, University of Washington, Seattle, Washington 98195, USA;*

E-mail: tangdd@uw.edu; lshen@bnu.edu.cn

Abstract

Fewest-switches surface hopping (FSSH) is the most popular method for simulating photochemical processes of molecular systems. Recently, we have constructed long short-term memory (LSTM) networks as a propagator for electronic subsystems in FSSH dynamics simulations. The collective results on Tully's three models have been reproduced satisfactorily. In the present work, we develop an extended LSTM-FSSH framework to simulate realistic photochemical reactions. The input features of LSTM as well as the training procedure are redesigned to represent high-dimensional nuclear degrees of freedom in an effective way. Equivariant neural networks are integrated with LSTM to build adiabatic potential energy surfaces in ground and excited states. Photoisomerizations of CH_2NH and azobenzene are simulated, showing that our new proposed LSTM-FSSH method can produce excited-state lifetimes and product yields accurately in comparison with conventional FSSH simulations as reference. Only 10 reference trajectories are required for training LSTM networks, and then a trajectory ensemble can be generated with very efficient LSTM-FSSH dynamics simulations to obtain collective results.

1 INTRODUCTION

Classical molecular dynamics simulations cannot study photochemical reactions because the Born-Oppenheimer approximation is no longer applicable in these cases. Fully quantum treatment on both nuclear and electronic degrees of freedom is too computationally expensive for realistic molecular systems, if not impossible. Mixed quantum classical molecular dynamics (MQC-MD) method, including Ehrenfest mean-field (EMF), surface hopping and ab initio multiple spawning (AIMS), provides a powerful tool to chemists. One of the most popular MQC-MD algorithms is the fewest switches surface hopping (FSSH)^{1,2} developed by Tully in 1990. During FSSH dynamic simulations, the nuclei move classically on an adiabatic potential energy surface (PES) with a certain probability of jumping to any other state. The transition probability is obtained based on the time evolution of electron density matrix, which incorporates quantum feedback of electronic motion. Despite its simple implementation and great success in many applications, the computational expense of FSSH remains much higher than that of ground-state MD. Not only the potential energies and gradients for all relevant electronic states but also the nonadiabatic coupling vectors (NACVs) between different states

should be calculated at a high level of electronic structure theory in each time step. Furthermore, FSSH requires an ensemble of trajectories to estimate collective results such as the excited-state lifetime and product yield. Strictly speaking, a dozen FSSH trajectories make little sense for revealing any mechanism of medium-sized or larger polyatomic molecules.

In recent years, there has been a growing interest in integrating machine learning (ML) techniques with MQC-MD for accelerating nonadiabatic dynamic simulations. ML has demonstrated its strong capability of fitting potential energy surfaces of high-dimensional molecules, either in the ground or excited state.³⁻⁷ However, accurate predictions of NACVs are much more difficult because the value of NACV often remains to be zero in most regions of PES but changes very suddenly around conical intersections, exhibiting significant scarcity and singularity characteristic. This problem may become more serious with the growth of molecule size and involved electronic states. Despite some great progress such as the combination of SchNet and SHARC,^{8,9} an alternative ML framework without the need of fitting NACVs is always attractive to the field of theoretical and computational photochemistry.

Cui, Lan, Wen and their co-workers have independently implemented the Zhu-Nakamura dynamic^{10,11} simulation on ML-based adiabatic PESs.¹²⁻¹⁵ Unlike FSSH, the transition probability can be estimated based on the Landau-Zener formalism, which only requires adiabatic energies and gradients. However, the difference between the collective results using FSSH and Zhu-Nakamura methods should be examined carefully when studying a new photochemical reaction. Rapid development on deep neural networks (NNs), such as long short-term memory (LSTM)¹⁶ and transformer,¹⁷ provides an opportunity to accelerate dynamic simulations by replacing the equation of motion with ML-predicted sequences. For time propagation of electronic degree of freedom, the history of density matrix can be considered as a time series and applied to LSTM or other NNs to predict the electron density matrix in the next

time step. For example, Lan and coworkers developed several LSTM models and successfully reproduced dynamics simulation results of the symmetrical quasi-classical dynamics method based on the Meyer-Miller mapping Hamiltonian (MM-SQC)¹⁸ and the full quantum multilayer multiconfiguration time-dependent Hartree (ML-MCTDH) method.¹⁹ Singh et al. employed Fourier neural operators as an effective time propagator of the MCTDH quantum dynamics for time-independent and time-dependent potentials.²⁰ Lin and Gao integrated convolutional neural networks and LSTM for prediction of open quantum dynamics under non-Markovian stochastic Schrödinger equation.²¹ Ullah et al. proposed physics-informed and Lie algebra-based approaches to recover exact trace conservation during ML-driven quantum dynamics.²² Sun and coworkers built different kinds of NNs and investigated the influence of neural network complexity on time evolution of electronic state population.²³ Recently, our group implemented LSTM as a propagator for electronic subsystem during the FSSH simulations.²⁴ The LSTM-FSSH satisfactorily reproduced collective results on Tully's three models.

Although the applications of ML-based propagators have covered from MM-SQC to ML-MCTDH, the study on realistic photochemical reactions is rare now. In comparison with other nonadiabatic dynamics methods, surface hopping is more suitable for simulating complex molecular systems. However, there are still two difficulties that impede further application of our constructed LSTM-FSSH framework. First, the dimensionality of nuclear subsystem varies in a broad range and sometimes significantly exceeds that of electronic subsystem. How to modelling the coupling between nuclear and electronic motions is not only the core of MQC-MD but also the key to the performance of ML prediction. The information about two subsystems should be both involved in LSTM as input features, but the balance point between the amounts of nuclear and electronic information is still being explored case by case. Second, the excited-state calculation on potential energies and gradients is a bottleneck for most photochemical reaction systems.

The combination of ML-based force fields and LSTM-FSSH provides a solution. However, the construction of ML-based potentials in excited states is much more challenging than that in the ground state, mainly due to the lack of reference values and the complexity of intersection regions on PESs.

In this work, we aim to solve the above problems and develop an extended LSTM-FSSH framework to simulate realistic photochemical reactions more effectively. The input features of LSTM were redesigned to represent high-dimensional nuclear degrees of freedom, and the procedure was modified to enhance training efficiency. The LSTM was further integrated with the NequIP model to build adiabatic PESs. The method will be described in Section 2. Then two photoisomerization reaction systems were employed to validate the performance of LSTM-FSSH. The results will be provided and compared with conventional FSSH simulations in Section 3, followed by conclusion and outlook in Section 4.

2 METHOD

2.1 Equivariant neural network

Conventional deep neural networks have been widely used to learn potential energy surfaces of diverse molecules,^{25,26} including photochemical reaction systems. Similarly, NequIP²⁷ also employs atomic types and coordinates as inputs, and then outputs molecular potential energies and gradients. The distinctive feature of NequIP lies in achieving equivariance through the utilization of equivariant convolutional layers, which aims at attaining corresponding alterations in the outcomes under symmetric operations. For instance, in the steerable E(3) equivariant graph neural networks, the forces on atoms are predicted directly.²⁸ If the molecular system rotates, the predicted atomic forces should also rotate accordingly, which represents equivariance. The strategy applied to NequIP is to encode the atomic positions and other feature information by means of spherical harmonic functions, followed by equivariant con-

volutional layers for information interaction to guarantee the realization of equivariance in the transmission of network information. A growing number of applications in various systems have demonstrated its superior accuracy, especially in absence of big data for training. Here we built NequIP to predict PESs of photochemical systems based on the e3nn library that merges recent progress on neural network models, such as tensor field networks,²⁹ 3D steerable convolutional neural networks,³⁰ and Clebsch-Gordan Nets.³¹ More details can be referred to the original literature.

2.2 FSSH method

In the FSSH method, the atomic nuclei move on a single potential energy surface in an adiabatic electronic state, which obeys the Newton's second law as

$$m_a \ddot{\mathbf{R}}_a = -\nabla_{\mathbf{R}_a} E_j(\mathbf{R}) \quad (1)$$

where E_j is the potential energy in the current (active) electronic state j , m_a is the mass of nucleus a , and \mathbf{R}_a is the Cartesian coordinates of nucleus a . The potential energies and the corresponding gradients (i.e., atomic forces) can be predicted using NequIP. On the other hand, the evolution of electronic degrees of freedom is determined by the time-dependent Schrödinger equation as

$$\dot{\rho}_{jk} = -\frac{i}{\hbar} \rho_{jk} (E_j - E_k) - \sum_l \dot{\mathbf{R}} \cdot (\mathbf{d}_{jl} \rho_{lk} - \rho_{jl} \mathbf{d}_{lk}) \quad (2)$$

where ρ_{jk} is the element of electron density matrix related to state j and k , and \mathbf{d}_{jk} is the nonadiabatic coupling vector between state j and k , which can be expressed as

$$\mathbf{d}_{jk}(\mathbf{R}) = \langle \psi_j(\mathbf{R}) | \nabla_{\mathbf{R}} | \psi_k(\mathbf{R}) \rangle \quad (3)$$

The evolution of electron density matrix determines the transition of nuclear motion from

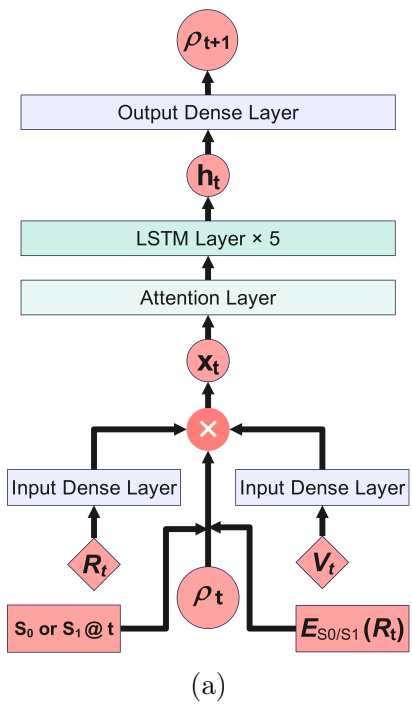
state j to k according to a probability $P_{j \rightarrow k}$ as

$$P_{j \rightarrow k}(t, t + \Delta t) = \max \left[0, \frac{\int_t^{t + \Delta t} 2 \operatorname{Re}(\dot{\mathbf{R}} \cdot \mathbf{d}_{jk} \rho_{kj}) d\tau}{\rho_{jj}(t)} \right] \quad (4)$$

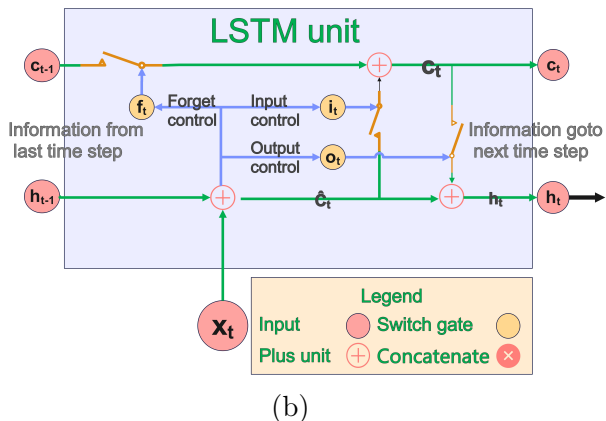
For two-state systems simulated in this work, the transition possibility can be written as

$$P_{j \rightarrow k}(t, t + \Delta t) = \max \left[0, \frac{\rho_{jj}(t + \Delta t) - \rho_{jj}(t)}{\rho_{jj}(t)} \right] \quad (5)$$

2.3 LSTM model



(a)



(b)

Figure 1: Framework (a) and unit (b) of LSTM network model.

LSTM can be considered as a functional formed by the composition of a specific mathematical operations. The total framework and a typical unit of the LSTM network model were shown in Figure 1. Based on the inputs x_t (processed via the first attention layer) in the current time step and the hidden variables h_{t-1} in the last step, three gates that control the “memory” during time evolution are employed as

$$f_t = \operatorname{sigmod}(\mathbf{W}_{fx} x_t + \mathbf{W}_{fh} h_{t-1} + \mathbf{B}_f) \quad (6)$$

$$i_t = \operatorname{sigmod}(\mathbf{W}_{ix} x_t + \mathbf{W}_{ih} h_{t-1} + \mathbf{B}_i) \quad (7)$$

$$o_t = \operatorname{sigmod}(\mathbf{W}_{ox} x_t + \mathbf{W}_{oh} h_{t-1} + \mathbf{B}_o) \quad (8)$$

Then the hidden variables h_t and memory cells c_t in the current step are calculated as

$$\tilde{c}_t = \tanh(\mathbf{W}_{cx} x_t + \mathbf{W}_{ch} h_{t-1} + \mathbf{B}_c) \quad (9)$$

$$c_t = f_t \odot c_{t-1} + i_t \odot \tilde{c}_t \quad (10)$$

$$h_t = \tanh(c_t) \odot \tilde{o}_t \quad (11)$$

where \odot denotes pointwise multiplication. The electron density matrix ρ_t is finally obtained from h_t via serval attention and dense layers, which are denoted as “Output Dense Layer” in Figure 1, as follows

$$\rho_{t+1} = f(\mathbf{W}_{yh} h_t + \mathbf{B}_y) \quad (12)$$

where f is an active function such as the sigmoid, tanh and rectified linear unit (ReLu) functions. In this work, we also built encoders in prior to the LSTM layers for dimensionality reduction extraction of input features. They are denoted as “Input Dense Layer” for simplicity in Figure 1. The detailed structures of LSTM networks and hyperparameters used in this work can be seen in Figure S1 and Table S1.

2.4 Input Features

How to represent the nuclear and electronic degrees of freedom with appropriate input features is the key to enhance the performance of LSTM predictions. For a low-dimensional system such as Tully’s three models, it is usually sufficient to apply some fundamental input features to LSTM, such as electron densities, po-

tential energies, nuclear coordinates and velocities. Modelling on realistic molecules is much more difficult. Here we proposed five groups of input features to simulate realistic photochemical reactions: atomic coordinates, atomic velocities, elements of electron density matrix, potential energy difference between electronic states and index of active electronic state.

2.4.1 SOAP Descriptors

The information of nuclear degrees of freedom is represented in the first and second groups of input features. The smooth overlap of atomic orbitals (SOAP) descriptor,^{32,33} which provides an elegant way for translation, rotation and permutation invariance of atoms, was employed in this work. The basic idea of the SOAP descriptor is to define the atomic density of the space using the Gaussian function, and then to expand it using a set of basis functions. On one hand, the density of an element with nuclear charge Z is

$$\rho^Z(\mathbf{r}) = \sum_i^{|Z|} e^{-\frac{1}{2\sigma^2}|\mathbf{r}-\mathbf{R}_i|^2} \quad (13)$$

where \mathbf{R}_i is the coordinate of atom i with nuclear charge Z , and σ is a pre-defined hyperparameter. Then the spherical harmonic (Y_{lm}) and radial Gaussian (g_n) basis functions are used to expand $\rho^Z(\mathbf{r})$ as

$$\rho^Z(\mathbf{r}) = \sum_{nlm} c_{nlm}^Z g_n(r) Y_{lm}(\theta, \varphi) \quad (14)$$

where c_{nlm}^Z is the coefficient and can be converted into the SOAP descriptors as

$$p_{nn'l}^{Z1, Z2} = \pi \sqrt{\frac{8}{2l+1}} \sum_m (c_{nlm}^{Z1})^* (c_{n'l'm}^{Z2}) \quad (15)$$

In this work, we built a set of SOAP descriptors directly to represent nuclear coordinates. The number of SOAP descriptors was set as $N \times N_{\text{SOAP}}$, where N is the total number of atoms. We also changed \mathbf{r} and \mathbf{R}_i in eq 13 to \mathbf{v} and \mathbf{V}_i , respectively, and built another set of input features to describe nuclear velocities

in each dynamic step. The min-max normalization was performed, in which the maximum and minimum values of each feature were derived from the training set. The normalized values were subsequently applied to the input dense layers for dimensionality reduction. In this work, we decreased the number of input features in the first group of as well as that in the second group from $N \times N_{\text{SOAP}}$ to a smaller N_{nuc} .

2.4.2 Electronic State Density

The information of electronic degrees of freedom is represented explicitly with electron density matrix. As discussed in our previous work, the diagonal elements of density matrix, which are relevant to the population of the simulated system on different electronic states, play the most essential role on the prediction performance of LSTM. On one hand, it has been observed that the LSTM-driven trajectory would fail very likely in presence of prediction deviations occurring around the value of 0.5. On the other hand, the activation functions are usually activated around zero. Consequently, we introduced a rescaling function g to diagonal elements of density matrix as eq 16 (see the next page), in which x denotes a diagonal element of density matrix. No rescale is applied to off-diagonal elements of density matrix since their characteristics is not difficult for training, at least in the present cases.

2.4.3 Potential Energy

The fourth and fifth groups of input features include more information of simulated systems during time propagation in an implicit way. The potential energy difference has a great influence on the evolution during surface hopping dynamics, especially once the transition event takes place. We applied $x_{\log \Delta E}$ and $x_{\Delta E^{-1}}$ as the fourth group of input features to capture the difference between E_{S_1} and E_{S_0} as

$$\begin{cases} x_{\log \Delta E} = \log_{10}(E_{S_1} - E_{S_0} + \epsilon) - 1 \\ x_{\Delta E^{-1}} = \frac{2.5}{(E_{S_1} - E_{S_0}) + 1} - 1 \end{cases} \quad (17)$$

$$g(x) = \begin{cases} \frac{0.05}{0.55 + (x - 0.5)}, & \text{if } x \leq 0.1 \\ \frac{19375}{576}(x - 0.5)^5 - \frac{925}{144}(x - 0.5)^3 + (x - 0.5), & \text{if } 0.1 \leq x \leq 0.9 \\ \frac{0.05}{0.55 - (x - 0.5)}, & \text{if } x \geq 0.9 \end{cases} \quad (16)$$

where E_{S_1} and E_{S_0} denote the potential energies in the S_1 and S_0 state, respectively, in unit of kcal/mol. ϵ is a small positive constant introduced to prevent numerical instability. The active electronic state is another key to surface hopping. In this work we simulated two-state systems, and thus the index of active state was set to -1 for the ground state and 1 for the excited state as the fifth group of input features.

2.4.4 Physical Constraint

In brief, the time-dependent information of nuclear and electronic degrees of freedom in several previous steps is embedded into input features of the LSTM model, and the elements of electron density matrix in the current step is predicted by LSTM. For two-state systems simulated in this work, the outputs of LSTM include ρ_{00} , ρ_{11} , $\text{Re}(\rho_{01})$ and $\text{Im}(\rho_{01})$. Until now, the physical constraints to electron density matrix are not considered during the modelling of LSTM. We addressed this issue after output dense layers of LSTM. First, the value of diagonal element should be recapped once it exceeds the range between 0 and 1, that is

$$\rho_{jj} := \begin{cases} 0 & \text{if } \rho_{jj} \leq 0 \\ 1 & \text{if } \rho_{jj} \geq 1 \end{cases} \quad (18)$$

Second, the trace of density matrix should be a constant of 1, leading to normalization to the predicted values as

$$\rho_{jj} := \frac{\rho_{jj}}{\sum_k \rho_{kk}} \quad (19)$$

Finally, the module of off-diagonal elements should match the module of diagonal elements. We have observed that violation of this constraint may result in some errors in the judg-

ment of surface hopping during long-term propagation. The following correction for a two-state system is performed as

$$\begin{cases} \text{Re}(\rho_{01}) := \text{Re}(\rho_{01}) \sqrt{\frac{\rho_{00}\rho_{11}}{|M_{01}|^2}} \\ \text{Im}(\rho_{01}) := \text{Im}(\rho_{01}) \sqrt{\frac{\rho_{00}\rho_{11}}{|M_{01}|^2}} \end{cases} \quad (20)$$

where ρ_{00} and ρ_{11} have been corrected in eqs 18 and 19, and $|M_{01}|$ is the module of ρ_{01} before correction.

2.5 Work procedure

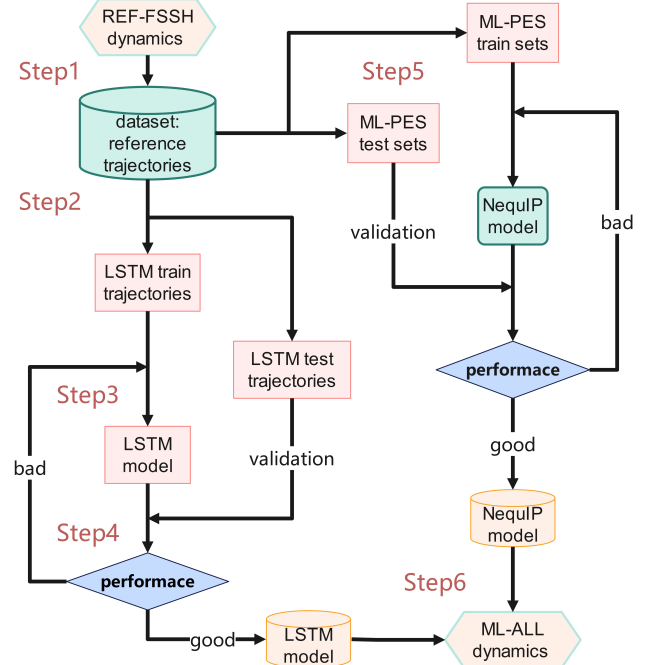


Figure 2: Workflow of combined LSTM and NequIP for FSSH simulations.

The whole process of this work was illustrated in Figure 2 and summarized as follows:

- (1) Perform conventional FSSH simulations on the selected photochemical reaction system with different random seeds. A small number

of reference trajectories were generated (e.g., 9 trajectories for CH_2NH and 10 trajectories for azobenzene) and further divided into training and test representative trajectories. For each trajectory, the atomic coordinates and velocities, electron density matrix, potential energies in all relevant electronic states as well as the gradients with respect to atomic coordinates, and the active electronic state in each dynamic step were recorded for ML modelling.

(2) Extract a time series of input features with M frames from one training trajectory as a sequence to build the LSTM model. Similar to our previous work, the sequence is shifted forward by M_{shift} frames until the end of this trajectory. This step is repeated across other training trajectories to extract a large number of sequences (e.g., 8 trajectories for CH_2NH yields 16,000 sequences and 9 trajectories for azobenzene yields 13,500 sequences).

(3) Construct an LSTM model based on the extracted sequences with a standard machine learning modelling procedure.

(4) Use the test trajectories (e.g., one representative trajectory for CH_2NH) to validate LSTM. For each selected trajectory, the initial M -length sequence consisting of all input features is applied to the constructed LSTM model, predicting the electron density matrix in the next step. Then the next M -length sequence, in which only the electron density matrix is replaced with the prediction result, is applied to LSTM iteratively. The LSTM model is acceptable if the LSTM-driven time evolution of electron density matrix is consistent with the corresponding reference result. Otherwise, go back to step 3 rebuild LSTM using different hyperparameters.

(5) Extract thousands of snapshots from all reference trajectories to build training and test sets of NequIP (e.g., 2,000 snapshots for CH_2NH from 9 trajectories). The snapshots populated in different electronic states are separated to build individual NequIP models for adiabatic PESs in each state. If the training loss or test MAE of the ML-PES model is unsatisfactory, we can consider expanding the snapshot dataset, adjusting the weights of energy and force terms in the loss function, or per-

forming additional targeted molecular dynamics simulations to sample new configurations in underrepresented regions.

(6) Combine the constructed NequIP and LSTM models to perform FSSH simulations on the selected photochemical reaction system. Nuclear degrees of freedom are still propagated according to the Newton's second law, but the potential energies and atomic forces are predicted with NequIP, avoiding expensive excited-state electronic structure calculations. Time evolution of electronic degrees of freedom are driven by LSTM without the need of nonadiabatic couplings. Collective results such as excited-state lifetime and photochemical product yield can be estimated based on hundreds or thousands of simulated trajectories.

There are two main differences between our previous work and this study. First, we introduced NequIP models to construct adiabatic PESs in all relevant electronic states, which is critical to save expensive computational cost on electronic structure calculations of realistic molecular systems. It should be noted that the test trajectories selected for validating LSTM should exhibit representative changes on density matrix, while the dataset for building NequIP should cover broad regions on PESs. It means that more dynamics trajectories may be required in order to obtain more accurate ML-PESs, especially for large molecules. Second, the validation of LSTM in step 4 changes from "on-the-fly" to "off-line". In our previous study on Tully's three models, LSTM-FSSH dynamic simulations were implemented under initial conditions and random numbers as the same as test trajectories. Time evolution of nuclear degrees of freedom would be affected by LSTM once a hopping event occurs. In this work, however, only the electron density matrix evolves with LSTM, while the atomic coordinates and velocities remain the same as those in the reference FSSH trajectories. Since the transition probability is determined by ρ_{jj} , the active state should be also influenced by LSTM, changing nuclear motion sequentially. Here we ignored such influence for simplicity as follows: when the index of active state in an LSTM-driven trajectory becomes different from its reference (i.e.,

representative trajectory), which is due to prediction errors on ρ_{jj} , the index of active state as the fifth group of input features would be determined by LSTM, but the nuclear motion (i.e., the first, second and fourth input features) would be subjected to the reference trajectory.

2.6 Simulation details

The first test system is the photoisomerization of CH₂NH along the central dihedral angle, starting from its S₁ state. In this work, all initial molecular configurations were defined artificially as the *cis*-isomer, and the *cis*- and *trans*-isomers were distinguished by a hydrogen atom labeled as H5 (see Figure 3a). We employed the complete active space self-consistent field (CASSCF) method with the basis set of 6-31G(d) for electronic structure calculations to generate reference FSSH dynamic trajectories in step 1. The active space consists of 2 electrons and 2 orbitals (π and π^*). The second test system is the *cis*-to-*trans* photoisomerization of azobenzene along \angle C-N-N-C, starting from its S₁ state (see Figure 3b). We applied OM2 Hamiltonian with the multi-reference configuration interaction (OM2/MRCI) method for electronic structure calculations to generate reference trajectories. An active space of 10 electrons in 8 orbitals was used, including four π orbitals, one n orbital and three π^* orbitals. The OpenMolcas³⁴ and MNDO programs³⁵ were used for CASSCF and OM2/MRCI^{36,37} calculations, respectively.

For each test system, 1,000 initial conditions were generated based on the Wigner sampling in 300 K using the corresponding module in the Newton-X program.³⁸ The integration time steps of the nuclear and electronic motions were set as 0.1 and 5×10^{-4} fs, respectively, for all nonadiabatic dynamic simulations. Total simulation time of each trajectory was 400 and 300 fs for CH₂NH and azobenzene, respectively. No decoherence correction was applied to FSSH in this work for simplicity. LSTM models were trained using Keras v2.13.1³⁹ combined with TensorFlow v2.13.0⁴⁰. Adiabatic PESs of these two systems were constructed with NequIP v0.6.1.^{27,41}

3 RESULTS AND DISCUSSION

3.1 Performance of NequIP models

We extracted 4,000 snapshots from the reference trajectories of CH₂NH and split them by 1:1 to generate the training and test sets to build the potential energy surfaces in its S₀ and S₁ states. As shown in Figures 4a and 4b, the prediction accuracy is good enough. The test mean absolute errors (MAEs) of $E(S_0)$ and $E(S_1)$ were 0.016 and 0.019 eV, respectively, with the force loss in the order of 10⁻² eV/Å. Key configurations observed in the reference trajectories, involving *cis*- and *trans*-isomers as well as minimum energy conical intersections, were shown in Figure S5a. Notably, a nitrene in which the H5 atom moves from nitrogen to carbon (see Figure S5b) also appeared in a few cases. It is more difficult for ML to accurately predict potential energies of such nitrene-like configurations in the high-energy region of PES. Although the performance of NequIP was robust, the influence of these nitrene-like configurations on dynamics simulations cannot be ignored at all times. We will discuss this issue later.

Because of the high-dimensional complexity of azobenzene, building accurate deep learning PESs is more challenging. To ensure sufficient sampling of the configurational space, we performed 20 more FSSH simulations at the OM2/MRCI computational level and extracted 4,000 snapshots from a total 30 reference trajectories. These snapshots were split to training and test sets to construct PESs. Key configurations related to photoisomerization of azobenzene can be seen in Figure S5c. As shown in Figure 4c and 4d, the performance of NequIP was acceptable. The MAEs of $E(S_0)$ and $E(S_1)$ on the test sets were 0.052 and 0.055 eV, respectively. The corresponding force loss per atom was increased to the order of 10⁻¹ eV/Å. On one hand, a larger dataset required to construct accurate PESs of azobenzene retards the efficiency of the whole procedure. With the de-

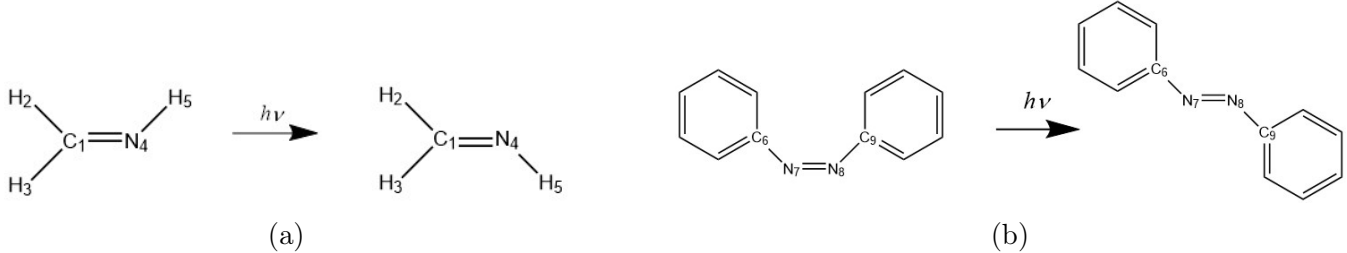


Figure 3: Photoisomerizations of CH_2NH (a) and azobenzene (b).

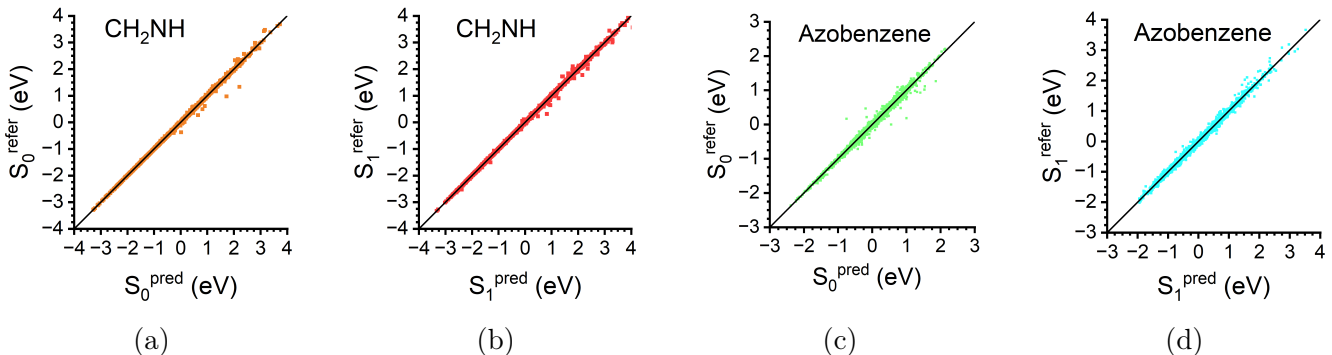


Figure 4: Comparisons between reference and NequIP-predicted potential energies for CH_2NH in S_0 (orange), CH_2NH in S_1 (red), azobenzene in S_0 (green), and azobenzene in S_1 (blue). Absolute values of potential energies have been shifted by a constant for clarity: 2,555 eV for CH_2NH in S_0 , 2,552 eV for CH_2NH in S_1 , 2,102 eV for azobenzene in S_0 , and 2,100 eV for azobenzene in S_1 .

development of deep learning potentials, however, we believe that the need of big data can be reduced using the pre-train-and-fine-tune strategy in the near future. On the other hand, 10 reference trajectories were sufficient for LSTM training on azobenzene (see below), which indicates potential superiority of LSTM on large molecular systems.

3.2 Representative trajectories

It has been observed previously that comparison between reference and predicted sequences is insufficient to validate the performance of LSTM because of the accumulated prediction errors during time evolution. Here we selected representative test trajectories for two test systems and examined time evolution of ρ_{00} driven by conventional FSSH or constructed LSTM. The time-dependent values of $x_{\log\Delta E}$ during LSTM-driven simulations were also detected because this input feature is relevant to a threshold of surface hopping. Any transition event would be rejected if the energy gap was

larger than 10 kcal/mol, corresponding to a positive value of $x_{\log\Delta E}$. In contrast, a very negative $x_{\log\Delta E}$ usually suggests strong coupling between two electronic states.

The simulation results of CH_2NH can be seen in Figure 5. We mainly focused on the significant coupling within the time intervals of 30-36, 52-60 and 75-105 fs. First of all, consistency between reference and LSTM trajectories around the time period of the first surface hopping is essential. As shown in Figure 5, both trajectories start in the S_1 state and firstly switch to the ground state at about 35 fs, exhibiting the same pattern of time evolution of ρ_{00} . Then the reference trajectory undergoes three frequent transitions between 52 and 60 fs, finally returning to S_1 . LSTM captures the second but misses the third and fourth hopping events. Within the time interval of 75-105 fs, the values of ρ_{00} strongly oscillate in both simulations, accompanied by an increasing deviation of LSTM from the reference data. Nevertheless, electron density matrix obtained using LSTM is comparable to the reference in the early stage of

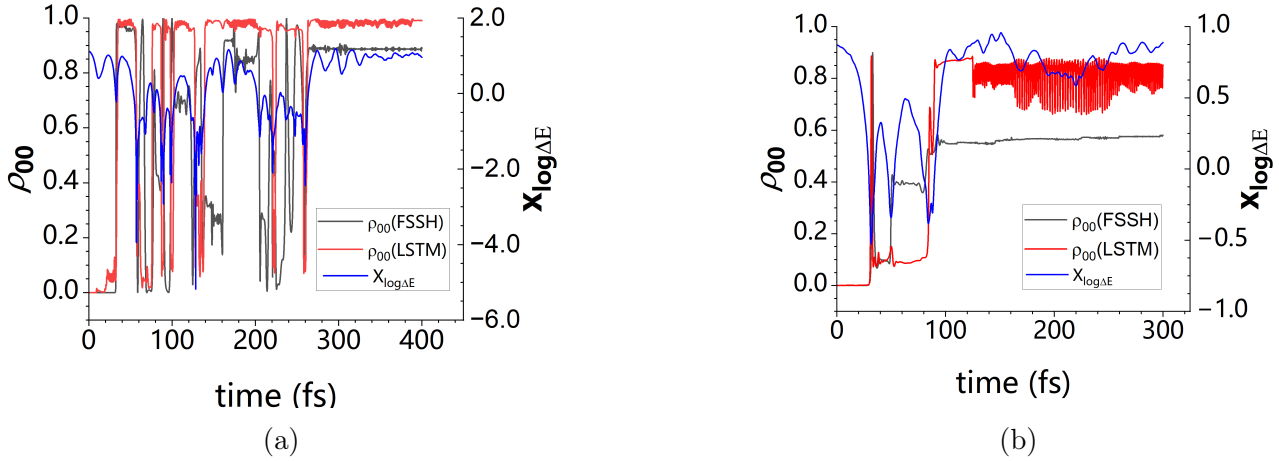


Figure 5: Population of ρ_{00} and $x_{\log\Delta E}$ as functions of time evolved in representative trajectories for CH₂NH (a) and azobenzene (b). Different colors represent different variables: ρ_{00} (FSSH) in black, ρ_{00} (LSTM) in red, and $x_{\log\Delta E}$ in blue.

dynamic simulation. The overall performance of LSTM after 105 fs is still acceptable. Notably, the overestimation of ρ_{00} between 130 and 140 fs may result in some decrease in simulated excited-state lifetime. Both trajectories converge to S₀ at the end of simulations.

Photoisomerization of azobenzene is a more challenging system for LSTM training because of its higher dimensionality. Similar to CH₂NH, more attention should be still paid to electronic motion in presence of strong coupling, especially around transition events in the early stage of simulations. As shown in Figure 5, the reference trajectory approaches the intersection vicinity at about 30, 50 and 85 fs, leading to a sudden change of ρ_{00} as well as surface hopping. LSTM reproduces the first two transitions occurring between 28 and 36 fs. Both trajectories switch from S₁ to S₀ and then back to S₁. However, LSTM trajectory remain in the excited state within 47-53 fs, which deviates from the reference trajectory and may attribute to the overestimated excited-state lifetime. LSTM also correctly responses to the strong coupling around 80-90 fs. Despite the difference of converged ρ_{00} between two simulations, both reference and LSTM trajectories decay to the ground state after 100 fs. The above performance of LSTM is acceptable for such a complicated system.

It should be noted that only a small portion

of LSTMs are able to reproduce the reference data qualitatively in our practice. A majority of constructed models clearly fail to pass the above validation on representative test trajectories. Some negative examples were summarized in Figures S2 and S3.

3.3 Collective results

We simulated independent dynamics trajectories under different initial conditions, i.e., 800 for CH₂NH and 1,000 for azobenzene, to obtain collective results. Three simulation methods denoted as REF-FSSH, ML-PES and ML-ALL were implemented individually. For each method, the total number of simulated trajectories has been enough to achieve converged collective results. As displayed in Figure S4, the excited-state lifetime collected from a smaller ensemble of 100 trajectories remains divergent. In comparison, our proposed LSTM requires only 10 reference trajectories for training but is able to produce hundreds of independent trajectories at very small cost.

REF-FSSH provides reference data in absence of any ML model. ML-PES employs our constructed NequIP models to predict potential energies and gradients in the ground and excited states. The nonadiabatic coupling vector was still calculated using the external QM program. In other words, electronic motion was

Table 1: Predicted excited-state lifetimes and photochemical product yields of photoisomerizations of CH_2NH and azobenzene using different simulation methods.

	System	REF-FSSH	ML-PES	ML-ALL
product yield (%)	CH_2NH	54.8 ± 1.1	49.9 ± 1.2	50.4 ± 1.2
	Azobenzene	45.9 ± 0.8	43.1 ± 0.9	45.6 ± 0.9
S_1 lifetime (fs)	CH_2NH	70.4 ± 1.4	80.4 ± 1.9	68.8 ± 1.0
	Azobenzene	88.2 ± 1.3	84.2 ± 1.3	91.4 ± 1.3

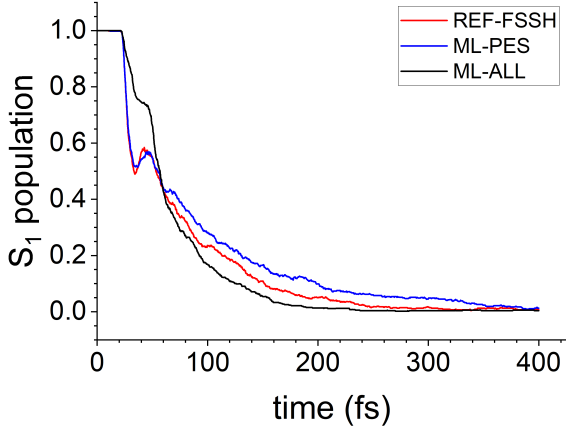
driven in the conventional way as REF-FSSH. ML-ALL is our proposed model that applies NequIP and LSTM to evolve nuclear and electronic degrees of freedom, respectively. Similar to our previous observations, 6~8 % of REF-FSSH trajectories failed because of unphysical dissociation of molecule. This problem appeared in 19% of CH_2NH and 17% of azobenzene trajectories when electronic structure calculation was replaced with NequIP. The former mainly originates from nitrene-like configurations, while the latter is caused by the difficulty in building ML-based PESs for large molecules. The failure percentage is still acceptable on account of much higher efficiency of ML predictions. The excited-state lifetime and photochemical product yield were collected from successful trajectories. The S_1 lifetime τ was obtained by fitting the time-dependent S_1 population as $P(t) = H(t_0 - t) + H(t - t_0)e^{-(t-t_0)/\tau_d}$, resulting in $\tau = t_0 + \tau_d$.

The time-dependent electronic state populations on the S_1 state of CH_2NH can be seen in Figure 6a. The result of ML-PES coincides with FSSH in the first 60 fs but exhibits a slight deviation subsequently. It might be due to the mismatch between adiabatic PESs and nonadiabatic couplings. The former was predicted approximately using NequIP, while the latter was obtained precisely using external electronic structure calculation programs. If the regions with strong nonadiabatic coupling do not match the regions where the corresponding potential energy difference is allowed, the transition from S_1 to S_0 that should occur would be blocked, leading to an increase in the lifetime of the excited state (70.4 fs with REF-FSSH and 80.4 fs with ML-PES, see Table 1). The S_1 lifetime

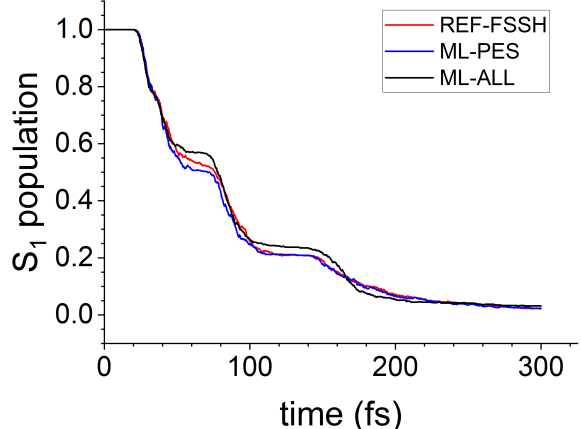
predicted with ML-ALL was 68.8 fs and very close to the reference value of 70.4 fs. However, error cancellation appears in the time-dependent S_1 population curve. The underestimation of LSTM is relevant to its transition pattern, such as broader distribution of hopping events on nuclear degrees of freedom and more rapid dynamic behavior around conical intersection. More details can be seen in Section 3.4.

As shown in Figure 6b, both ML-PES and ML-ALL applied to azobenzene can reproduce the reference curve of its time-dependent S_1 population. The corresponding simulations lead to the lifetime of 84.2 and 91.4 fs, respectively, which were in good agreement with the REF-FSSH prediction of 88.2 fs. Notably, the lifetime of excited azobenzene was slightly underestimated by ML-PES while overestimated by ML-ALL, which was opposite to CH_2NH . The former might be due to different potential energy gaps in strong coupling regions, which would be further discussed in Section 3.4. The latter can be explained based on the representative test trajectory shown in Section 3.2. Notably, the first plateau in the S_1 population curve may correspond to the sudden change of electron density matrix around 50 fs during simulations. It was missed out in the LSTM-driven test trajectory, making the system stay in the excited state longer.

Photochemical product yields of two reactions were estimated according to the molecular configurations in the last simulation step of total trajectories. The *cis*-to-*trans* transformation of CH_2NH is determined by artificially marking the hydrogen atom connected to the nitrogen. The product yields were predicted as 0.55, 0.50



(a)



(b)

Figure 6: Population of the electronic states S_1 during photoisomerization of CH_2NH (a) and azobenzene (b). Different colors represent different methods: REF-FSSH in red, ML-PES in blue, and ML-ALL in black.

and 0.50 with REF-FSSH, ML-PES and ML-ALL, respectively. Note that a small deviation from 0.50 can be attributed to the occurrence of nitrene-like configurations. The photochemical product yields of *cis*-azobenzene were predicted as 0.46, 0.43 and 0.46 using REF-FSSH, ML-PES and ML-ALL, respectively. Our proposed ML method can accurately reproduce photoreaction yields of realistic molecules, at least for the present test examples.

3.4 Distribution of hopping events

To better demonstrate the reliability of our proposed ML framework, the distribution of hopping events from S_1 to S_0 was mapped to low-dimensional space. The results of different simulation methods were shown in Figure 7. The density of dots indicates the probability of surface hopping, while the color represents the value of potential energy gap between S_0 and S_1 .

Observations on the hopping events during photoisomerization process of CH_2NH were in good agreement with the collective results. Firstly, we focused on the dots with larger $\angle \text{C1-N4-H5}$. The energy gaps were increased in presence of ML, making an incongruence between the intersection of PESs and the region with

strong nonadiabatic coupling. During ML-PES simulations, it finally led to less frequent transitions to the ground state as well as the overestimated excited-state lifetime. However, the influence on ML-ALL simulations is opposite. Unlike ML-PES in which electron density matrix evolves based on the calculated d_{jk} , ML-ALL disregarded nonadiabatic coupling vectors and predicted the change of ρ_{00} directly, enabling surface hopping more rapidly once the system approaches the intersection region. It does not only led to the underestimation of lifetime with LSTM but also resulted in the broader distribution of hopping events.

Additionally, the dots with smaller $\angle \text{C1-N4-H5}$ in Figure 7a correspond to nitrene-like configurations of CH_2NH . These short-lived configurations appear infrequently in a single trajectory but can be sampled in many trajectories in the REF-FSSH dynamics. On one hand, the dynamic behavior of ML-PES in the region is similar to that of REF-FSSH, indicating good performance of NequIP in a broad configurational space. On the other hand, the training of LSTM becomes much more challenging in presence of these configurations, which may result in fewer hopping events in the region using ML-ALL. Nevertheless, the occurrence of nitrene-like configurations may lead to unstable dynamic trajectories, which would be excluded

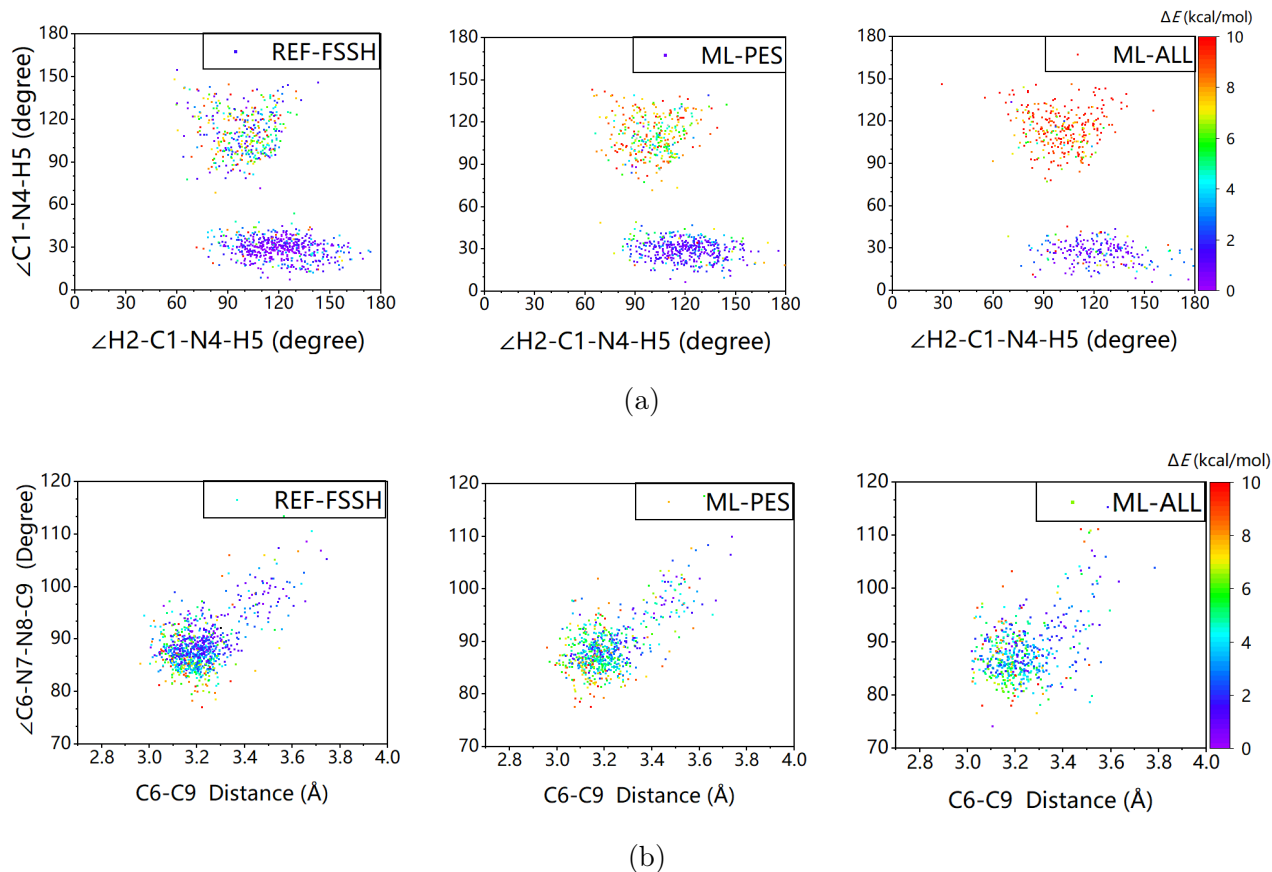


Figure 7: Distributions of hopping events during photoisomerizations of CH_2NH (a) and azobenzene (b) using REF-FSSH (left), ML-PES (middle), and ML-ALL (right). Different colors represent different values of $E_{\text{S}1} - E_{\text{S}0}$ when transition event occurs.

from collective results. The influence can be thus ignored in the present case.

The hopping events during photoisomerization of *cis*-azobenzene can be seen in Figure 7b. Similar to Figure 7a, the use of NequIP increased the potential energy gap in the coupling region. However, most of transitions took place when the energy gap was smaller than 5 kcal/mol. It is quite different from the dynamic behavior of CH_2NH , in which a hopping attempt with an energy gap near 10 kcal/mol was often observed. As mentioned above, such transitions would be rejected during ML-PES simulations of CH_2NH . In contrast, most of hopping attempts were accepted for azobenzene because of smaller energy gaps. Thus, the deviation of ML-predicted S_1 lifetime of azobenzene can be neglected compared to that of CH_2NH .

As observed in Figure 7 and in our previous work, the performance of ML is prone to deteriorate around conical intersections. A weighted

sampling related to potential energy difference should be useful when selecting training points from reference trajectories. However, whether the additional samplings are really effective remains to be studied on realistic molecules. It would be difficult to determine an appropriate weight in prior if multiple relaxation channels should be considered. Inclusion of rare configurations may seriously impede the training of LSTM models, such as the case of CH_2NH discussed above. We will take care of these issues in the future.

4 CONCLUSIONS AND OUTLOOK

In this work, we constructed a machine learning framework that consists of the NequIP potential energy surface prediction model and the LSTM electron density evolution predic-

tion model. Starting from our previous work, the input features and modelling procedure of LSTMs were significantly modified for high-dimensional systems. It was successfully applied to fewest switches surface hopping, which is the most widely used nonadiabatic dynamic method, to simulate realistic molecules. Aside from NequIP for fitting adiabatic PESs, LSTM acts as the time propagator of electronic degrees of freedom, providing an alternative solution to deal with nonadiabatic couplings as the key to surface hopping. We employed two typical photochemical systems as CH_2NH and azobenzene, and validated that the proposed ML models can produce S_1 lifetimes and product yields satisfactorily in comparison with conventional FSSH simulations. Despite the high dimensionality of molecular systems, only 10 reference trajectories were sufficient for LSTM training, followed by very efficient ML-driven dynamic simulations to generate trajectory ensemble.

There is much room for improvement. First, the construction of excited-state PESs, even if without the need of fitting nonadiabatic coupling, is more challenging than that in the ground state. The success of ML-based PESs on excited CH_2NH has been demonstrated in recent years, while the complexity of ML algorithms is more essential to excited-state dynamic simulations on azobenzene as well as its derivatives. Although deep learning techniques such as SchNet and NequIP have exhibited their advantage according to our experience, the trade-off between computational accuracy and overhead remains a nontrivial issue, especially when dealing with larger molecules. OMNI-P2x^{42,43} and other Δ -learning⁴⁴ models may provide alternatives to our future work. Second, the validation of LSTM models in step 4 is the bottleneck of the whole procedure. Similar to our previous work, here we still compared the time evolution of ρ_{00} in representative test trajectories visually, which depends on our prior understanding of simulated systems. More rigorous and automated analysis method is necessary. Additionally, only a few LSTM models built in step 3 (e.g., 4% for azobenzene) can exhibit superior performance, leading to a cumbersome iteration between check-

ing and rebuilding. How to enhance the success rate of LSTM training is important to achieve higher efficiency. For instance, our designed input features of LSTM can be replaced with an equivariant network in principle. It exceeds our scope of this work. Finally, applications on more diverse systems are attractive but require modifications on the present framework. For example, the transition probability in eq 5 cannot deal with photochemical processes involving more than two electronic states. The global flux surface hopping⁴⁵ algorithm developed by Wang and coworkers offers a potential solution, but the growing size of electron density matrix would lead to more outputs of LSTMs and more complex network structures. Generalization of LSTM-driven surface hopping for simulating both internal conversion and intersystem crossing processes on an equal footing seems to be straightforward. However, intersystem crossing is always a rare event compared to internal conversion around conical intersections, posing a significant challenge for LSTM training.

Supporting Information

Introduction and details of NequIP, details of LSTM, negative examples for validation of representative trajectories, and supplemental results of two photochemical systems.

Conflict of Interest

The authors declare no conflict of interest.

Data Availability

The source code is available on <https://github.com/uminominami/LSTM-NequIP-code-v1>

Acknowledgements

We are grateful to the financial support from the Natural Science Foundation of China (22573008, 22193041 and 22288201) and the

References

(1) Tully, J. C. Molecular dynamics with electronic transitions. *J. Chem. Phys.* **1990**, *93*, 1061–1071.

(2) Hammes-Schiffer, S.; Tully, J. C. Proton transfer in solution: Molecular dynamics with quantum transitions. *J. Chem. Phys.* **1994**, *101*, 4657–4667.

(3) Behler, J.; Parrinello, M. Generalized Neural-Network Representation of High-Dimensional Potential-Energy Surfaces. *Phys. Rev. Lett.* **2007**, *98*, 146401.

(4) Wang, H.; Zhang, L.; Han, J.; E, W. DeePMD-kit: A deep learning package for many-body potential energy representation and molecular dynamics. *Comput. Phys. Commun.* **2018**, *228*, 178–184.

(5) Dral, P. O. MLatom: A program package for quantum chemical research assisted by machine learning. *J. Comput. Chem.* **2019**, *40*, 2339–2347.

(6) Westermayr, J.; Marquetand, P. Machine Learning for Electronically Excited States of Molecules. *Chem. Rev.* **2021**, *121*, 9873–9926.

(7) Kulichenko, M. et al. Data Generation for Machine Learning Interatomic Potentials and Beyond. *Chem. Rev.* **2024**, *124*, 13681–13714.

(8) Westermayr, J.; Gastegger, M.; Menger, M. F. S. J.; Mai, S.; González, L.; Marquetand, P. Machine learning enables long time scale molecular photodynamics simulations. *Chem. Sci.* **2019**, *10*, 8100–8107.

(9) Westermayr, J.; Gastegger, M.; Marquetand, P. Combining SchNet and SHARC: The SchNarc Machine Learning Approach for Excited-State Dynamics. *J. Phys. Chem. Lett.* **2020**, *11*, 3828–3834.

(10) Zhu, C.; Nakamura, H. Theory of nonadiabatic transition for general two-state curve crossing problems. I. Nonadiabatic tunneling case. *J. Chem. Phys.* **1994**, *101*, 10630–10647.

(11) Zhu, C.; Nakamura, H. Theory of nonadiabatic transition for general two-state curve crossing problems. II. Landau–Zener case. *J. Chem. Phys.* **1995**, *102*, 7448–7461.

(12) Chen, W.-K.; Liu, X.-Y.; Fang, W.-H.; Dral, P. O.; Cui, G. Deep Learning for Nonadiabatic Excited-State Dynamics. *J. Phys. Chem. Lett.* **2018**, *9*, 6702–6708.

(13) Hu, D.; Xie, Y.; Li, X.; Li, L.; Lan, Z. Inclusion of Machine Learning Kernel Ridge Regression Potential Energy Surfaces in On-the-Fly Nonadiabatic Molecular Dynamics Simulation. *J. Phys. Chem. Lett.* **2018**, *9*, 2725–2732.

(14) Xu, H. et al. Ultrafast Photocontrolled Rotation in a Molecular Motor Investigated by Machine Learning-Based Nonadiabatic Dynamics Simulations. *J. Phys. Chem. A* **2023**, *127*, 7682–7693.

(15) Xu, W.; Xu, H.; Zhu, M.; Wen, J. Ultrafast dynamics in spatially confined photoisomerization: accelerated simulations through machine learning models. *Phys. Chem. Chem. Phys.* **2024**, *26*, 25994–26003.

(16) Hochreiter, S.; Schmidhuber, J. Long Short-Term Memory. *Neural Computation* **1997**, *9*, 1735–1780.

(17) Vaswani, A. et al. Attention Is All You Need. 2023; <https://arxiv.org/abs/1706.03762>.

(18) Lin, K.; Peng, J.; Xu, C.; Gu, F. L.; Lan, Z. Trajectory Propagation of Symmetrical Quasi-classical Dynamics with Meyer-Miller Mapping Hamiltonian Using Machine Learning. *J. Phys. Chem. Lett.* **2022**, *13*, 11678–11688.

(19) Lin, K.; Peng, J.; Gu, F. L.; Lan, Z. Simulation of Open Quantum Dynamics with Bootstrap-Based Long Short-Term Memory Recurrent Neural Network. *J. Phys. Chem. Lett.* **2021**, *12*, 10225–10234.

(20) Singh, K.; Lee, K. H.; Peláez, D.; Bande, A. Accelerating wavepacket propagation with machine learning. *J. Comput. Chem.* **2024**, *45*, 2360–2373.

(21) Lin, K.; Gao, X. Simulating Open Quantum Dynamics with a Neural Network-Enhanced Non-Markovian Stochastic Schrödinger Equation. *J. Chem. Theory Comput.* **2025**, *21*, 5803–5814.

(22) Ullah, A.; Richardson, J. O. Machine learning meets $su(n)$ Lie algebra: Enhancing quantum dynamics learning with exact trace conservation. *J. Chem. Phys.* **2025**, *162*, 244106.

(23) Wu, D.; Hu, Z.; Li, J.; Sun, X. Forecasting nonadiabatic dynamics using hybrid convolutional neural network/long short-term memory network. *J. Chem. Phys.* **2021**, *155*, 224104.

(24) Tang, D.; Jia, L.; Shen, L.; Fang, W.-H. Fewest-Switches Surface Hopping with Long Short-Term Memory Networks. *J. Phys. Chem. Lett.* **2022**, *13*, 10377–10387.

(25) Schütt, K.; Kindermans, P.-J.; Sauceda Felix, H. E.; Chmiela, S.; Tkatchenko, A.; Müller, K.-R. SchNet: A continuous-filter convolutional neural network for modeling quantum interactions. Advances in Neural Information Processing Systems. 2017.

(26) Schütt, K. T.; Sauceda, H. E.; Kindermans, P.-J.; Tkatchenko, A.; Müller, K.-R. SchNet – A deep learning architecture for molecules and materials. *J. Chem. Phys.* **2018**, *148*, 241722.

(27) Batzner, S. et al. E(3)-equivariant graph neural networks for data-efficient and accurate interatomic potentials. *Nat. Commun.* **2022**, *13*, 2453.

(28) Brandstetter, J.; Hesselink, R.; van der Pol, E.; Bekkers, E. J.; Welling, M. Geometric and Physical Quantities Improve E(3) Equivariant Message Passing. 2022; <https://arxiv.org/abs/2110.02905>.

(29) Thomas, N. et al. Tensor field networks: Rotation- and translation-equivariant neural networks for 3D point clouds. 2018; <https://arxiv.org/abs/1802.08219>.

(30) Weiler, M.; Geiger, M.; Welling, M.; Boomsma, W.; Cohen, T. 3D Steerable CNNs: Learning Rotationally Equivariant Features in Volumetric Data. 2018; <https://arxiv.org/abs/1807.02547>.

(31) Kondor, R.; Lin, Z.; Trivedi, S. Clebsch-Gordan Nets: a Fully Fourier Space Spherical Convolutional Neural Network. 2018; <https://arxiv.org/abs/1806.09231>.

(32) Bartók, A. P.; Kondor, R.; Csányi, G. On representing chemical environments. *Phys. Rev. B* **2013**, *87*, 184115.

(33) Himanen, L. et al. Dscribe: Library of descriptors for machine learning in materials science. *Comput. Phys. Commun.* **2020**, *247*, 106949.

(34) Li Manni, G. et al. The OpenMolcas Web: A Community-Driven Approach to Advancing Computational Chemistry. *J. Chem. Theory Comput.* **2023**, *19*, 6933–6991.

(35) Thiel, W. MNDO program, version 8.0. Software, 2019.

(36) Weber, W. OM2. Ph.D. thesis, University of Zurich, 1996.

(37) Weber, W.; Thiel, W. Orthogonalization corrections for semiempirical methods. *Theor. Chem. Acc.* **2000**, *103*, 495–506.

(38) Barbatti, M. et al. Newton-X Platform: New Software Developments for Surface Hopping and Nuclear Ensembles. *J. Chem. Theory Comput.* **2022**, *18*, 6851–6865.

(39) Chollet, F.; others Keras. <https://keras.io>, 2015; Software.

(40) Abadi, M.; others TensorFlow: Large-Scale Machine Learning on Heterogeneous Systems. <https://www.tensorflow.org/>, 2015; Software.

(41) Geiger, M. et al. e3nn/e3nn: 2021-05-04 (0.2.9). 2021; <https://doi.org/10.5281/zenodo.4735637>.

(42) Martyka, M.; Tong, X.-Y.; Jankowska, J.; Dral, P. OMNI - P2x: A Universal Neural Network Potential for Excited - State Simulations. 2025; <https://doi.org/10.26434/chemrxiv-2025-j207x>.

(43) Martyka, M. et al. Charting electronic-state manifolds across molecules with multi-state learning and gap-driven dynamics via efficient and robust active learning. *npj Comput. Mater.* **2025**, *11*, 132.

(44) Ramakrishnan, R.; Dral, P. O.; Rupp, M.; von Lilienfeld, O. A. Big Data Meets Quantum Chemistry Approximations: The Δ -Machine Learning Approach. *J. Chem. Theory Comput.* **2015**, *11*, 2087–2096.

(45) Wang, L.; Trivedi, D.; Prezhdo, O. V. Global Flux Surface Hopping Approach for Mixed Quantum-Classical Dynamics. *J. Chem. Theory Comput.* **2014**, *10*, 3598–3605.

Supporting Information:

Fewest-Switches Surface Hopping with

Combined Deep Learning Potential and Long

Short-Term Memory Network Propagator for

Simulating Realistic Photochemical Processes

Zhenxing Zhu,[†] Diandong Tang,^{*,‡} Lin Shen,^{*,†} and Wei-Hai Fang[†]

[†]*Key Laboratory of Theoretical and Computational Photochemistry of Ministry of Education, College of Chemistry, Beijing Normal University, Beijing 100875, China;*

[‡]*Department of Chemistry, University of Washington, Seattle, Washington 98195, United States;*

E-mail: tangdd@uw.edu; lshen@bnu.edu.cn

Table of Contents

- Section S1. Introduction and details of NequIP
- Section S2. Details of LSTM
 - Table S1. Hyperparameters used for LSTM
 - Fig S1. Detailed structure of LSTM networks. N denotes the number of atoms.
- Section S3. Negative examples for validation of representative trajectories
 - Fig S2. Negative examples for validation of a representative trajectory of CH_2NH .
 - Fig S3. Negative examples for validation of a representative trajectory of azobenzene.
- Section S4. Supplemental Results
 - Fig S4. Convergence of trajectory ensembles using different FSSH methods
 - Fig S5. Key configurations in photoisomerization of CH_2NH and azobenzene

1 Introduction and details of NequIP

In this work, we employed the Neural E(3)-equivariant Interatomic Potential (NequIP) to build potential energy surfaces (PESs) in ground and excited states for dynamics simulations. Conventional neural networks (NNs) for PES construction are typically designed to be invariant under rotations and translations, often relying on handcrafted descriptors such as interatomic distances. Although this ensures invariance of the final output, the internal representation cannot transform in a physically consistent way under symmetry operations, limiting its ability to capture directional dependencies and geometric structure. In contrast, not only the total potential energy but also the atomic forces predicted by equivariant neural networks are invariant under rotation and translation. If the atomic coordinates are rotated, the forces rotate accordingly.

Unlike many NN-based potentials that rely on rotationally invariant scalar descriptors such as interatomic distances or angles, NequIP operates directly on relative position vectors pointing from atom i to atom j as

$$\vec{r}_{ij} = \vec{r}_i - \vec{r}_j \quad (\text{S1})$$

which preserves directional information and enables the network to capture anisotropic interactions. Such directional information is further mapped into spherical harmonic space, forming a complete basis for irreducible representations of the SO(3) group, and decomposing angular dependencies into well-defined angular momentum channels. The convolutional kernels in NequIP can be subsequently built as the product of a learnable radial function and the spherical harmonic basis function:

$$S_m^{(l)}(\vec{r}_{ij}) = R(r_{ij}) Y_m^{(l)}(\hat{r}_{ij}), \quad (\text{S2})$$

where r_{ij} and \hat{r}_{ij} denote the length and unit vector of \vec{r}_{ij} , respectively, $Y_m^{(l)}(\hat{r}_{ij})$ is the spherical harmonic function, and $R(r_{ij})$ is the radial function modeled by a multilayer perceptron. This factorization separates radial and angular degrees of freedom explicitly, ensuring that the

filter responses transform covariantly under 3D rotations.

Based on the spherical harmonic filters, the features in NequIP are propagated through equivariant tensor products as the following layer:

$$V_{\text{out}}^{(l_o, p_o)} \propto \sum_{b \in \mathcal{N}(i)} \sum_{m_i, m_f} C_{l_i m_i l_f m_f}^{l_o m_o} Y_{m_f}^{(l_f)}(\hat{r}_{ib}) R(r_{ib}) V_b^{(l_i, p_i)}. \quad (\text{S3})$$

Similar to the angular momentum theory in quantum mechanics, the Clebsch-Gordan (CG) coefficients serve here as the coupling constants that govern how irreducible representations of $\text{SO}(3)$ combine under tensor products. The equivariance of this operation is obvious: the entire framework, which encodes directional information into spherical harmonics and combines angular channels via the CG coefficients, is built upon a mathematical formalism that inherently respects 3D rotational symmetry. This tensor product layer also provides a mechanism to dynamically adjust the feature dimensions. By selecting which output channels to include, the network can expand or compress the representation across layers. For example, high-rank tensor features with $l \geq 2$ can be gradually reduced to vectors ($l = 1$) or scalars ($l = 0$) in the last layer, enabling a symmetry-preserving dimensionality reduction.

After multiple layers of equivariant message passing as above, the high-dimensional tensor features $V_i^{(l, p)}$ associated with atom i are gradually transformed and eventually projected down to the desired output space. In the NequIP for predicting potential energies, all features are reduced to scalar ($l = 0$) via an equivariant readout process. If only the invariant scalars are retained in the last layer, the total potential energy can be obtained by summing over these atomic contributions

$$E = \sum_i \alpha_i^{(0)} \cdot V_i^{(0)} \quad (\text{S4})$$

where $\alpha_i^{(0)}$ denotes learnable weights. It is worth noting that while the total potential energy is a rotationally invariant scalar, the internal representation throughout the above network consists of non-trivial high-order geometric tensors, which transform covariantly under $\text{E}(3)$ operations. Alternatively, some other equivariant NNs directly predict atomic forces as

vector outputs with $l = 1$, in which a rotation of the input structure induces a corresponding rotation of the force vectors.

Unlike conventional NNs that always discard angular information via scalarization at the beginning, NequIP preserves directional information and propagates it across layers, capturing complex angular dependencies with fewer training samples. By embedding physical symmetries directly into the network architecture, NequIP achieves superior generalization from limited data no more than a few thousand training configurations, and produces physically consistent predictions across diverse chemical environments from isolated molecules to extended periodic materials. For rigorous mathematical derivations and proofs of equivariant NNs, we refer the reader to the original papers about tensor field networks,^{S1} 3D steerable convolutional neural networks,^{S2} and Clebsch-Gordan Nets.^{S3}

The NequIP models used in this work consist of 4 interaction blocks with irreducible representations up to $l_{\max} = 2$ of spherical harmonics for encoding. The cutoff distance for message passing was set to be 4.0 Å. The batch size and initial learning rate for optimization were 5 and 0.01, respectively, accompanied with early stopping based on the validation loss with a patience of 1000 epochs, the maximum allowed validation loss of 10^4 , and the minimum allowed learning rate of 10^{-6} . The loss weights for potential energy and atomic forces were set as 1.0 and 0.1, respectively.

2 Details of LSTM

The structure of our proposed LSTM model was shown in Figure S1. As mentioned in the main text, the input features include nuclear coordinates, nuclear velocities, elements of electron density matrix, potential energies, and index of active state. Consider a two-state photochemical reaction with N atoms. The size of nuclear coordinate features is $M \times N \times N_{SOAP}$, where M denotes the length of previous time series extracted from dynamic trajectory, and N_{SOAP} is determined by the hyperparameters of SOAP (n_{max} and l_{max}). The size of nuclear velocity features is the same. The nuclear coordinate and velocity features are independently processed by an encoder, leading to a set of hidden variables with a reduced size of $M \times N_{nuc}$. The current encoder consists of the first dense layer with N_{den1} nodes, a reshape layer, and the second dense layer with N_{den2} nodes. Two sets of $M \times N_{nuc}$ hidden variables and the remaining input features are subsequently concatenated. Since two electronic states are involved in the present simulations, four elements of electron density matrix, two inputs derived from potential energies, and one index of active state should be considered. Thus, the size of the output of encoder is $M \times (2 \times N_{nuc} + 7)$. Then the variables are successively processed via the first attention layer with N_{atten1} heads, five LSTM layers with N_{LSTMx} ($x = 1-5$) nodes, the third dense layer with N_{den3} nodes, the second attention layer with N_{atten2} heads, a reshape layer and the fourth dense layer with N_{den4} nodes, leading to the predicted elements of electron density matrix in the next time step. $tanh$ was employed as the activation function of dense layers. The values of all hyperparameters used in this work were listed in Table S1.

Unlike conventional ML training procedures in which the prediction accuracy of test samples (i.e., a time series of density matrix in this work) should be examined carefully, reproduction of representative trajectories with the trained LSTM is much more important to validate ML performance. In this work, we paid less attention to the training procedure in order to reduce computational cost, especially for high-dimensional realistic molecular systems. In Step 3, we first performed several rounds (e.g., 4 for CH_2NH and 6 for azobenzene)

of LSTM training. After the preliminary optimization on LSTM parameters, we continued to train and saved the LSTM models every round. For each set of hyperparameters, 15 LSTM models with different parameters were saved. Finally, we picked one model with the smallest loss from them to validate whether the representative trajectories can be reproduced. On account of the fact that only a small portion of LSTMs are able to reproduce the reference trajectories, the above strategy is essential to enhance the efficiency of ML modelling. In contrast, all attempts on fine-tuning on optimizers were ineffective in practice. We applied the default Adam optimizer with batch size of 6 and learning rate of 10^{-3} in this work.

Table S1: Hyperparameters used for LSTM

Hyperparameter				Value	Description
SOAP	r_{cut}	4	cutoff radius for local chemical environment in unit of Å		
	σ	1.0	variance of Gaussian function for atomic density in unit of Å		
	n_{max}	2	number of radial basis functions		
	l_{max}	1	maximum degree of spherical harmonics		
		42	number of SOAP descriptors		
Encoder	N_{den1}	3	size of the first dense layer for encoding		
	N_{den2}	15	size of the second dense layer for encoding		
	N_{nuc}	15	dimensionality of nuclear DoFs after encoding ($= N_{\text{den2}}$)		
LSTM	N_{atten1}	4	number of heads in the first attention block		
	N_{LSTMx}	96	size of the x -th LSTM layer, $x = 1 \sim 5$		
	N_{den3}	4	size of the third dense layer after LSTM processing		
	N_{atten2}	4	number of heads in the second attention block		
	N_{den4}	4	size of the last dense layer ($=$ dimensionality of electronic DoFs)		
	M	32	number of frames in a sequence (time series) for training		
	M_{shift}	2	sequence shift for extracting the next sequence		

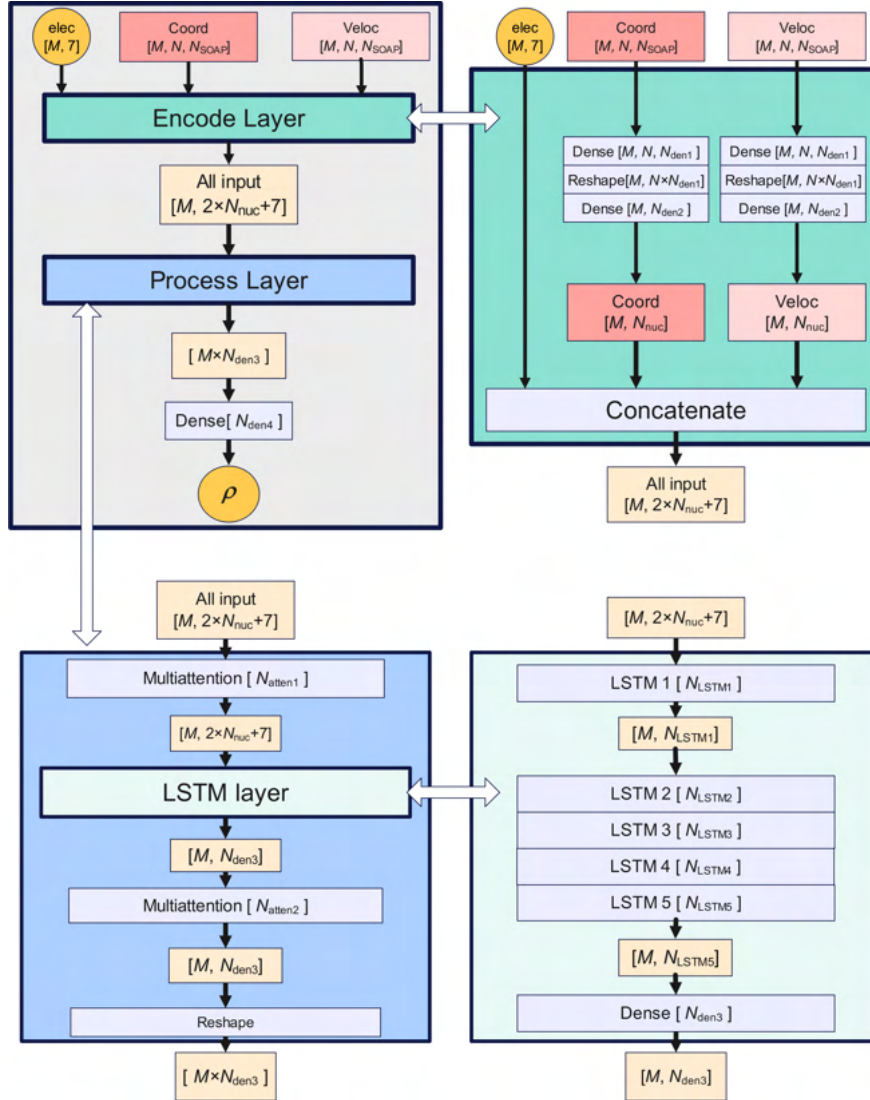


Figure S1: Detailed structure of LSTM networks. N denotes the number of atoms. M denotes the number of frames in a sequence (i.e., sequence length).

3 Negative examples for validation of representative trajectories

As discussed in the main text, only a small portion of LSTMs are able to reproduce the representative trajectory. In absence of a quantitative criterion to measure the similarity of two FSSH trajectories, we have no choice but to perform such comparisons visually and laboriously.

For two-state nonadiabatic processes, we focus on the time evolution of ρ_{00} . On account of the correction of eq 20 in the main text, the prediction accuracy of off-diagonal elements of density matrix mainly depends on the performance of ρ_{00} . Fortunately, most of negative results of ρ_{00} are easy to identify. Some negative examples of CH₂NH were listed in Figure S2, which can be excluded as follows:

- (1) The trivial trajectory without any change of ρ_{00} throughout dynamic simulations should be excluded firstly, such as (b) and (l).
- (2) The trajectory that jumps to other electronic state at the very beginning of simulations should be excluded, such as (c), (d), (e), (f), (g), (h), (j), (k) and (o). Obviously, these trajectories would deviate from the reference throughout dynamic simulations.
- (3) The trajectory missing the first hopping event indicates overestimation of excited-state lifetime, such as (a) and (n). The relevant LSTM is slightly better than those in (1) and (2). If the LSTM-driven trajectory exhibits similar pattern to the reference in the latter stage of dynamic simulation, the LSTM can be employed as the initial model for further optimization.
- (4) The trajectory that reproduces the first hopping event but exhibits a different pattern is better than those in (1), (2) and (3). However, we observed that the final collective results obtained using the corresponding LSTMs are still deviated from the reference values. For example, the oscillation after 50 ps in the reference trajectory is completely lost in (i) but overestimated in (m). Further optimization starting from these LSTMs is strongly suggested.

Negative examples of azobenzene were shown in Figure S3. Two thirds of them stay in the S_1 state throughout dynamic simulations. No transition takes place in these trajectories, making a serious mistake compared to the reference. The remaining trajectories capture the first hopping to the ground state at 20 fs, including (a), (b), (l) and (n). The re-hopping event back to the excited state, which is observed immediately in the reference trajectory, vanishes in (l) and appears too late in (b); (a) and (b) also undergo too frequent transitions between two states before 100 fs. Among these five trajectories, (a), (b) and (l) finally relax to the ground state as the same as the reference. None of them leads to satisfactory collective results during the following LSTM-driven dynamic simulations. Only (a) performs slightly better than others.

According to our experience, hundreds of attempts are necessary to obtain the best LSTM model with satisfactory reproducibility (as shown in Figure 5 in the main text). The use of more sophisticated NNs for PES construction can increase the successful rate, especially for medium-size or larger molecules. Fortunately, the training and validation processes have been modified in this work, reducing the computational cost significantly. As a result, so many visual comparisons are tedious for researchers but affordable for computational resources.

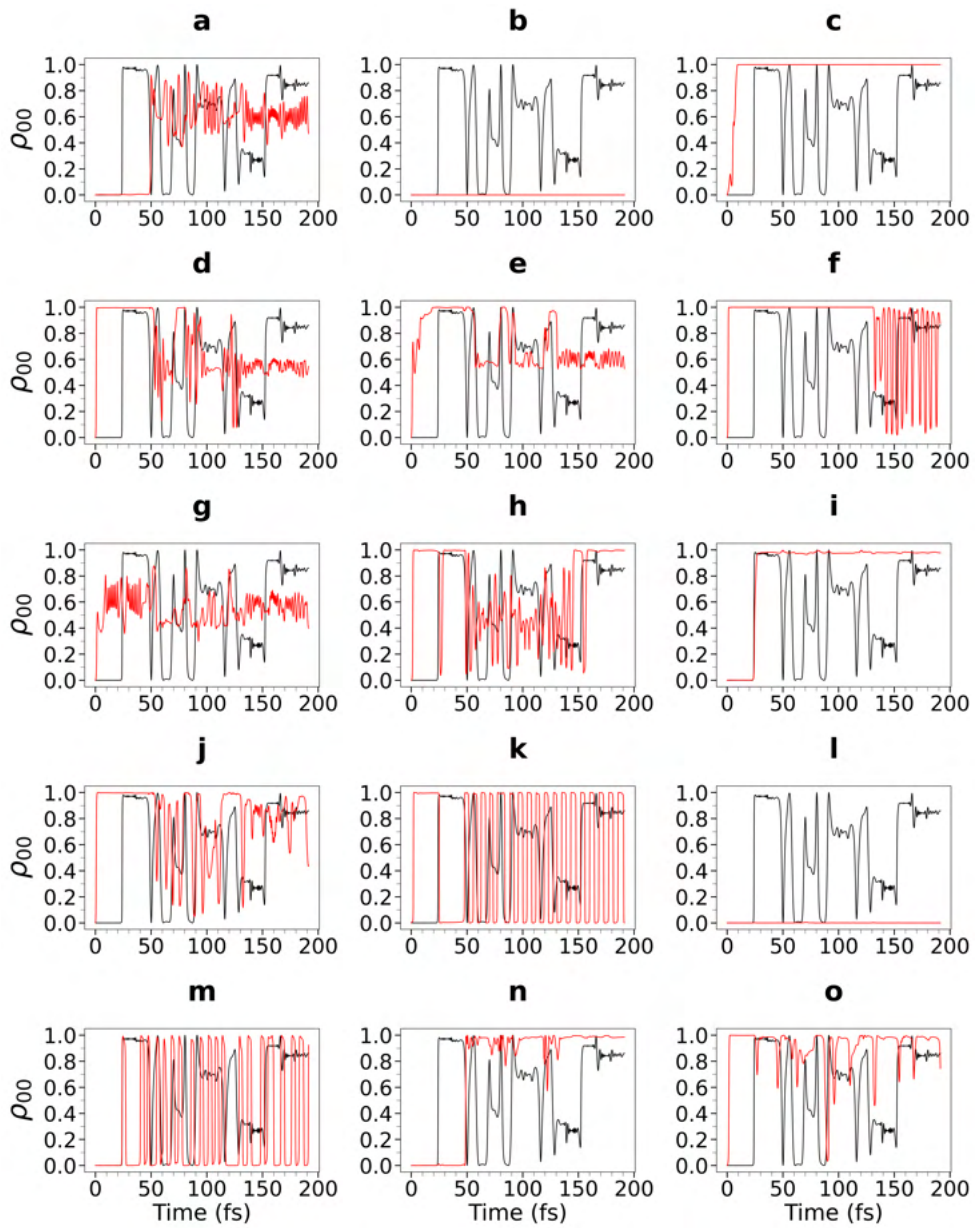


Figure S2: Negative examples for validation of a representative trajectory of CH_2NH . Different colors represent different methods: reference FSSH in black, LSTM-FSSH in red.

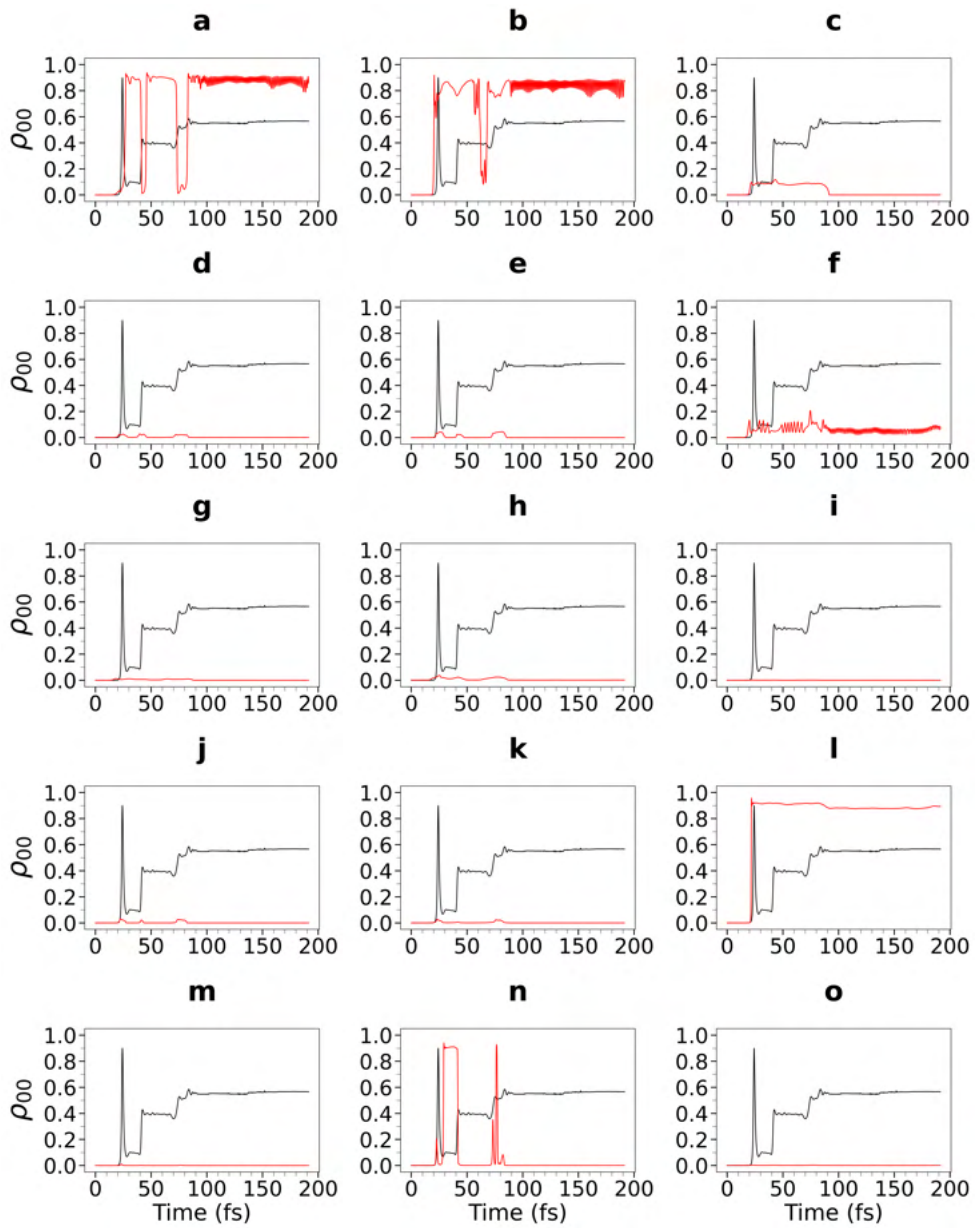


Figure S3: Negative examples for validation of a representative trajectory of azobenzene. Different colors represent different methods: reference FSSH in black, LSTM-FSSH in red.

4 Supplemental Results

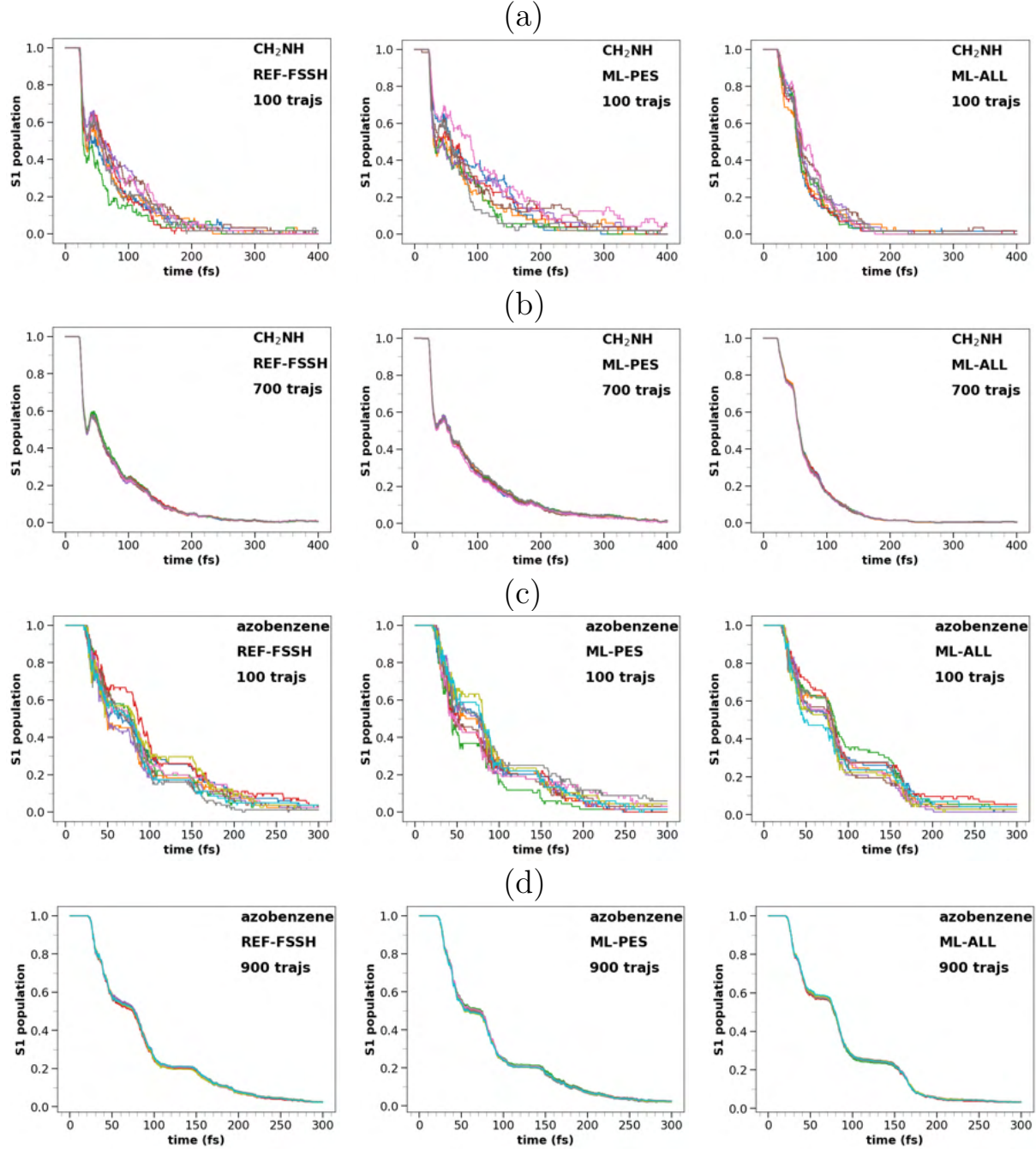


Figure S4: Convergence of trajectory ensembles. For FSSH simulations of CH_2NH , when 100 trajectories are selected from 800, the time-dependent S_1 state populations are divergent (a). In contrast, when 700 are selected from 800, the result achieves good convergence (b). Similarly, for simulations of azobenzene, when 100 trajectories are selected from 1000, the time-dependent S_1 state populations are divergent (c). In contrast, when 900 are selected from 1000, the result achieves good convergence (d).

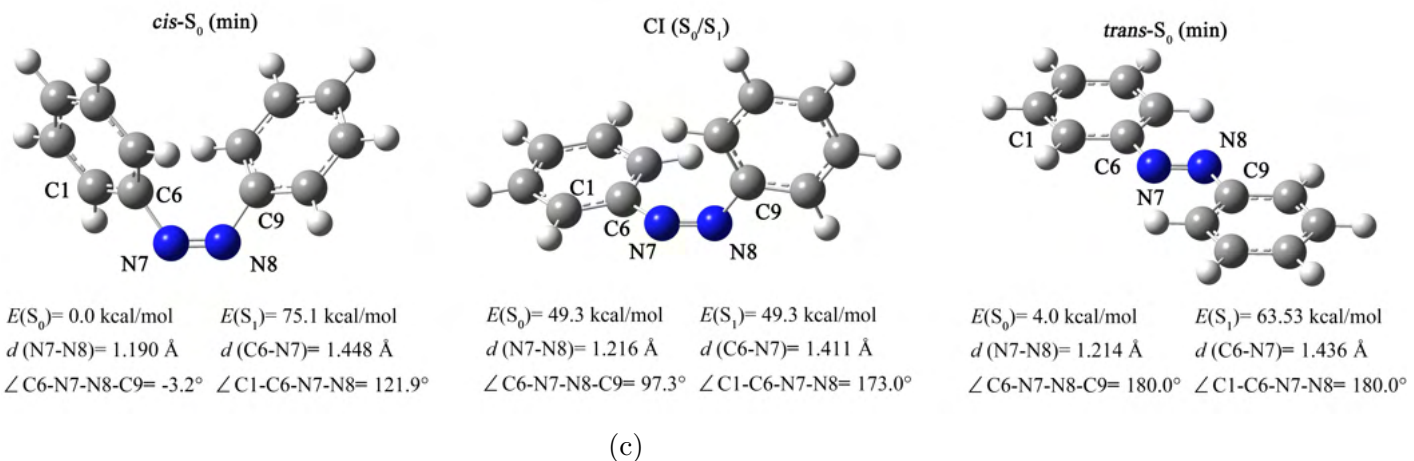
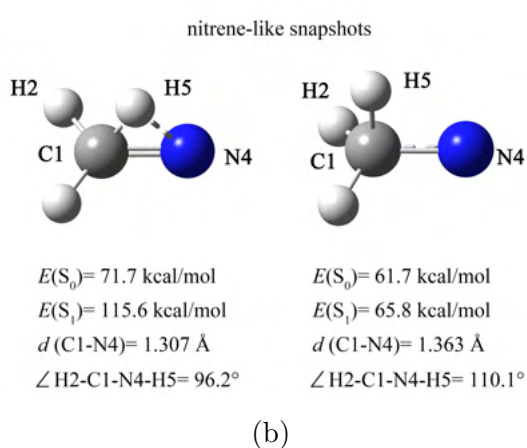
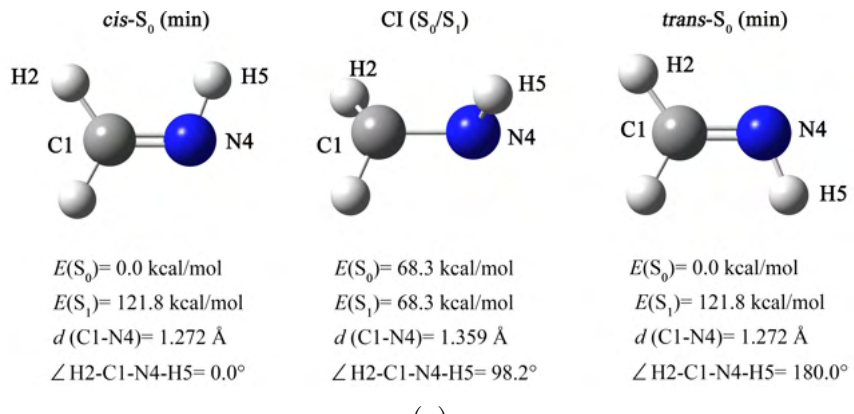


Figure S5: Key configurations with potential energies of two test systems: minima and conical intersection of CH_2NH optimized at the CASSCF(2,2)/6-31G(d) level (a), representative nitrene-like configurations of CH_2NH extracted from trajectories (b), minima and conical intersection of azobenzene optimized at the OM2/MRCI level (c).

References

- (S1) Thomas, N. et al. Tensor field networks: Rotation- and translation-equivariant neural networks for 3D point clouds. 2018; <https://arxiv.org/abs/1802.08219>.
- (S2) Weiler, M.; Geiger, M.; Welling, M.; Boomsma, W.; Cohen, T. 3D Steerable CNNs: Learning Rotationally Equivariant Features in Volumetric Data. 2018; <https://arxiv.org/abs/1807.02547>.
- (S3) Kondor, R.; Lin, Z.; Trivedi, S. Clebsch-Gordan Nets: a Fully Fourier Space Spherical Convolutional Neural Network. 2018; <https://arxiv.org/abs/1806.09231>.